Bio-Design and Manufacturing (2025) 8:656–671
https://doi.org/10.1631/bdm.2500061

RESEARCH ARTICLE

Microneedle-loaded hybrid extracellular vesicles promote diabetic wound healing

Yue Sun[1,2,3,4] · Qirong Zhou[5] · Shihao Sheng[5] · Huijian Yang[6] · Long Bai[1,2,3] · Zhen Geng[1,2,3] · Jian Wang[1,2,3] · Ke Xu[1,2,3] · Xiao Chen[5] · Yingying Jing[1,2,3] · Guangchao Wang[5] · Jiacan Su[1,2,3,5]

Received: 10 February 2025 / Accepted: 13 February 2025

Abstract

Chronic diabetic wounds result from a disrupted microenvironment where oxidative stress, impaired angiogenesis, and persistent infection create a vicious cycle that delays healing. Unfortunately, existing treatments often fail to address these interrelated issues, resulting in suboptimal healing. Here, we propose a base-tip dual-component hydrogel microneedle (MN) system (GBEVs-pVEGF/AgNPs@MNs), consisting of a tip loaded with plant-bacterial hybrid extracellular vesicles (GBEVs-pVEGF) and a base containing silver nanoparticles (AgNPs). Upon penetrating the necrotic tissue of diabetic wounds, our multifunctional MNs could effectively deliver GBEVs-pVEGF, thereby alleviating oxidative stress, promoting cell migration, and facilitating angiogenesis. Additionally, the physical barrier formed by the basal layer synergistically mitigates persistent bacterial infections during wound healing in conjunction with the antimicrobial agent AgNPs. This multifunctional MN system, integrating antioxidant, angiogenic, and antimicrobial properties, effectively restores the disrupted wound microenvironment, offering significant potential for accelerating diabetic wound healing.

Yue Sun, Qirong Zhou, Shihao Sheng, and Huijian Yang have contributed equally to this work.

✉ Xiao Chen
sirchenxiao@126.com

✉ Yingying Jing
jingy4172@shu.edu.cn

✉ Guangchao Wang
wgc@shsmu.edu.cn

✉ Jiacan Su
drsujiacan@163.com

[1] Institute of Translational Medicine, Shanghai University, Shanghai 200444, China

[2] Organoid Research Center, Shanghai University, Shanghai 200444, China

[3] National Center for Translational Medicine (Shanghai) SHU Branch, Shanghai University, Shanghai 200444, China

[4] School of Medicine, Shanghai University, Shanghai 200444, China

[5] Department of Orthopedics, Xinhua Hospital Affiliated to Shanghai Jiao Tong University School of Medicine, Shanghai 200092, China

[6] Department of Clinical Laboratory, Shanghai Zhongye Hospital, Shanghai 200941, China

Graphical abstract

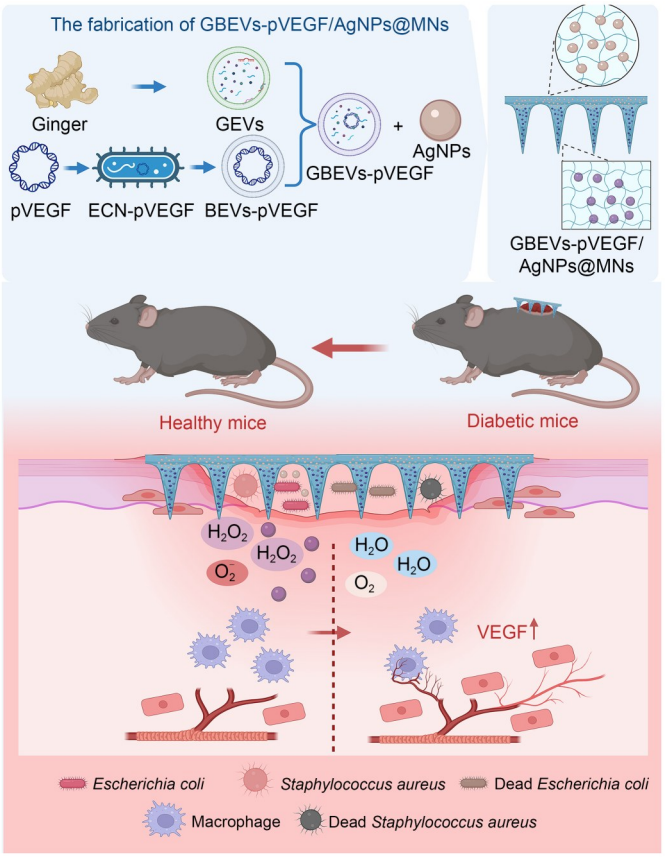

Keywords Extracellular vesicles (EVs) · Silver nanoparticles (AgNPs) · Microneedles (MNs) · Drug release · Diabetic wound healing

1 Introduction

Diabetic wounds, a prevalent chronic complication of diabetes, characterized by delayed healing, persistent infection, and alarmingly high mortality rates, are a significant health concern worldwide [1–3]. Despite the implementation of therapeutic interventions such as pharmacotherapy, surgical debridement, and antibiotic administration, the efficacy remains suboptimal [4, 5]. In the context of diabetic chronic wound healing, hyperglycemia is a pivotal factor influencing healing [6]. Hyperglycemia increases reactive oxygen species (ROS) levels, directly having cytotoxic effects on tissues and hindering angiogenesis, thereby compromising the blood supply required for wound repair [7, 8]. Moreover, hyperglycemia fosters a milieu that promotes bacterial proliferation, thereby increasing the susceptibility to infection [9]. In addition, chronic infection activates ROS production, worsening tissue damage and inhibiting vascular regeneration [10, 11]. Consequently, there is an urgent demand for safe and efficacious therapeutic interventions that target chronic diabetic wounds through triple mechanisms: exerting antioxidant effects, inhibiting bacterial proliferation, and promoting angiogenesis.

Extracellular vesicles (EVs) are nanoscale vesicles secreted by living cells known for their excellent biocompatibility and high drug-loading capacity [12]. Mammalian EVs are recognized for their diversity, targeting ability, and therapeutic potential, but the complex purification process and low yield limit their application [13–16]. The discovery of plant EVs and bacterial extracellular vesicles (BEVs) has, to some extent, overcome these challenges, offering new possibilities for promoting wound healing [17–19]. In addition, ginger-derived extracellular vesicles (GEVs) exhibit high extraction efficiency and yield, along with potent antioxidant properties, effectively modulating oxidative stress [20, 21]. However, GEVs demonstrate limited angiogenic capacity in the diabetic wound microenvironment, restricting this application.

The "gut-skin axis hypothesis" was first proposed, elucidating the potential correlation between the gut microbiota and cutaneous inflammation [22]. Subsequent research has shown that the gut microbiota regulates glucose metabolism and insulin sensitivity, with dysbiosis significantly contributing to diabetes [23, 24]. A significant member of the gut microbiota, *Escherichia coli* (*E. coli*) Nissle 1917 (ECN), is characterized by its amenability to genetic manipulation and scalability for large-scale fermentation [25]. ECN produces EVs through an explosive cell lysis mechanism, enabling these vesicles to carry components identical to those within the bacteria, allowing for customized production of engineered BEVs [26, 27]. To address the insufficient vascularization in diabetic wounds and the lack of genetic programmability of GEVs, we constructed a shuttle plasmid, the plasmid vascular endothelial growth factor (pVEGF), and introduced it into the ECN, ultimately generating a custom ECN. Using conventional culture methods rather than a two-step temperature regulation strategy, we effectively suppressed pVEGF expression during BEVs formation, thereby enabling the successful preparation of pVEGF-loaded BEVs (BEVs-pVEGF) [28]. Once internalized by the cells, the pVEGF in BEVs-pVEGF is expressed as VEGF, promoting angiogenesis. Therefore, to address the elevated ROS levels and insufficient angiogenesis, we developed plant-bacteria hybrid EVs (GBEVs-pVEGF) using a continuous extrusion-based membrane fusion approach inspired by the liposome-exosome fusion technology [29]. By integrating the antioxidant properties of GEVs with the proangiogenic capabilities of BEVs-pVEGF, this innovative strategy offers a comprehensive and promising solution for diabetic wound treatment. Nonetheless, the rapid loss of EVs from the skin surface generally limits their effectiveness [30, 31]. To address this issue, microneedles (MNs) have gained attention as a minimally invasive drug delivery tool. MNs can penetrate necrotic tissue in chronic wounds, directly delivering GBEVs-pVEGF to deeper sites, enhancing targeting and agent release [32–34]. Silver nanoparticles (AgNPs), as a widely utilized nanoscale antimicrobial agent, exhibit broad-spectrum and long-lasting antibacterial and antifungal efficacy [35, 36]. By incorporating AgNPs into the basal layer, their antimicrobial properties can synergize with the intrinsic physical barrier of the basal layer to effectively counteract bacterial infections during the wound healing process.

In this study, we developed a novel base-tip dual-component hydrogel MN system (GBEVs-pVEGF/AgNPs@MNs) to address the elevated ROS levels, insufficient vascularization, and persistent bacterial infections typical of diabetic wounds (Scheme 1). The GBEVs-pVEGF loaded at the MN tip can reduce ROS levels by releasing bioactive substances, wherein the pVEGF is expressed as VEGF within the cells, thereby combining the antioxidant properties of GEVs with the proangiogenic potential of BEVs-pVEGF. In addition, the inherent physical barrier of the MN basal layer synergizes with AgNPs to effectively mitigate bacterial infections. These multifunctional MNs specifically target the core pathological issues of diabetic wounds, offering a significant strategic reference for accelerating diabetic wound healing.

2 Results and discussion

2.1 Fabrication and characterization of GBEVs-pVEGF

BEVs-pVEGF were successfully isolated after semicontinuous fermentation and ultracentrifugation. Subsequently, GBEVs-pVEGF were fabricated by fusing GEVs and BEVs-pVEGF through low-speed ultrasonication combined with serial extrusion (Fig. 1a). Transmission electron microscopy (TEM) images showed that GBEVs-pVEGF exhibited a uniform spherical structure and maintained a stable phospholipid bilayer membrane structure (Fig. 1b). In addition, nanoparticle tracking analysis (NTA) indicated an intermediate particle size of the fused GBEVs-pVEGF ((173.2± 5.7) nm) between that of GEVs ((189.3±2.8) nm) and BEVs-pVEGF ((156.1±3.8) nm) (Fig. 1c). Fusion efficiency and membrane stability may have limited the extent of fusion, resulting in GBEVs-pVEGF with a particle size smaller than that of GEVs but larger than that of BEVs-pVEGF. Zeta potential measurements indicated that GBEVs-pVEGF, GEVs, and BEVs-pVEGF exhibited distinct surface charge values, with GBEVs-pVEGF having an intermediate value between GEVs and BEVs-pVEGF. These differences reflect changes in membrane composition following fusion (Fig. 1d).

To confirm the fusion of the two types of EVs, GEVs and BEVs-pVEGF were labeled with 3,3′-dioctadecyloxacarbocyanine perchlorate (DiO) and 1,1′-dioctadecyl-3,3,3′, 3′-tetramethylindocarbocyanine perchlorate (DiI) dyes, respectively (Fig. 1e). Confocal microscopy revealed significant DiO and DiI colocalization in GBEVs-pVEGF after serial extrusion, but no overlap in nonfused EVs. These results demonstrate that serial extrusion effectively enabled the membrane fusion of GEVs and BEVs-pVEGF.

2.2 Characterization of GBEVs-pVEGF/AgNPs@MNs

Scanning electron microscopy (SEM) images revealed that alginate methacryloyl (AlgMA), AgNPs/AlgMA, and GBEVs-pVEGF/AlgMA hydrogels (Fig. 2a) exhibited similar porous structures, with no significant differences in pore size or distribution. This indicates that the incorporation of AgNPs and GBEVs-pVEGF did not alter the original pore characteristics of the AlgMA hydrogel. This is important as the unchanged pore structure after loading small molecules

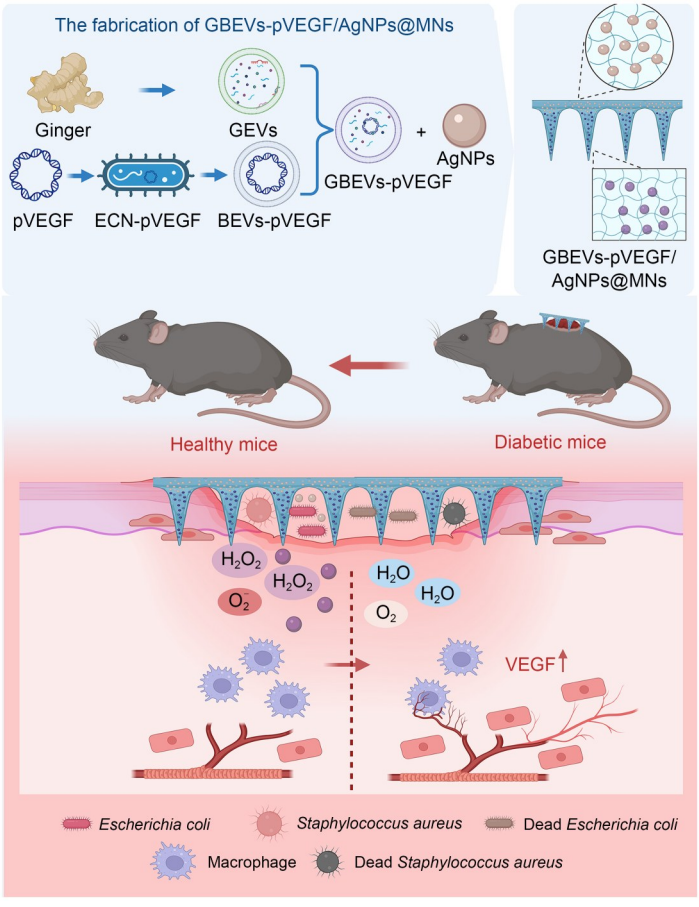

Scheme 1 Fabrication of GBEVs-pVEGF/AgNPs@MNs for accelerating diabetic wound healing. Multifunctional hydrogel MNs comprising an AgNP-containing base and a GBEVs-pVEGF-containing tip accelerate diabetic wound healing due to their antioxidant, antibacterial, and angiogenic effects

allows for sustained molecular release and efficient therapeutic efficacy [37, 38]. Further, energy dispersive spectroscopy (EDS) analysis confirmed successful GBEVs-pVEGF loading, with a strong phosphorus (P) signal originating from the phospholipid bilayer of the EVs (Fig. 2b). These results demonstrate that AgNPs and GBEVs-pVEGF can be efficiently loaded into the hydrogel without compromising its microstructure or functionality.

Optical microscopy (Fig. 2c) and SEM images (Fig. 2d) revealed that GBEVs-pVEGF/AgNPs@MNs exhibited a well-aligned MN array with solid tips, capable of effectively penetrating the skin. Swelling analysis showed that GBEVs-pVEGF/AgNPs@MNs rapidly reached stability (within 3 h), indicating excellent water uptake (Fig. 2e). In addition, rheological measurements (Fig. 2f) revealed that the storage modulus (G') of the AlgMA hydrogel exceeded the loss modulus (G''), demonstrating solid-like behavior and ensuring mechanical stability. Together, these results demonstrate that GBEVs-pVEGF/AgNPs@MNs exhibit excellent drug release capacity, rapid water absorption, and mechanical stability, making them suitable for diabetic wound healing.

2.3 Antioxidant assessment of GBEVs-pVEGF/AgNPs@MNs

The biocompatible concentration of AgNPs in the hydrogel MN base was 200 μg/mL as observed with Calcein acetoxymethyl ester/propidium iodide (Calcein AM/PI) staining (Fig. S1 in the supplementary information). Next, the biocompatibility of GBEVs-pVEGF/AgNPs@MNs was evaluated. Neither Calcein AM/PI staining (Fig. 3a; Fig. S2 in the supplementary information) nor cell counting kit-8 (CCK-8) assays (Figs. 3d and 3e) showed significant cytotoxicity following GBEVs-pVEGF/AgNPs@MNs treatment, confirming the cellular safety of GBEVs-pVEGF/AgNPs@MNs. Since EVs can regulate recipient cells by transferring bioactive molecules [39, 40], we assessed the internalization, by introducing DiD-labeled GBEVs-pVEGF into the cells. Uptake experiments (Fig. 3b) confirmed substantial GBEVs-pVEGF absorption, demonstrating their capability to deliver biomolecules to target cells.

Bioactive compounds with antioxidant properties in ginger, such as gingerol and shogaol, could provide the same properties to GBEVs-pVEGF/AgNPs@MNs [41, 42]. Thus,

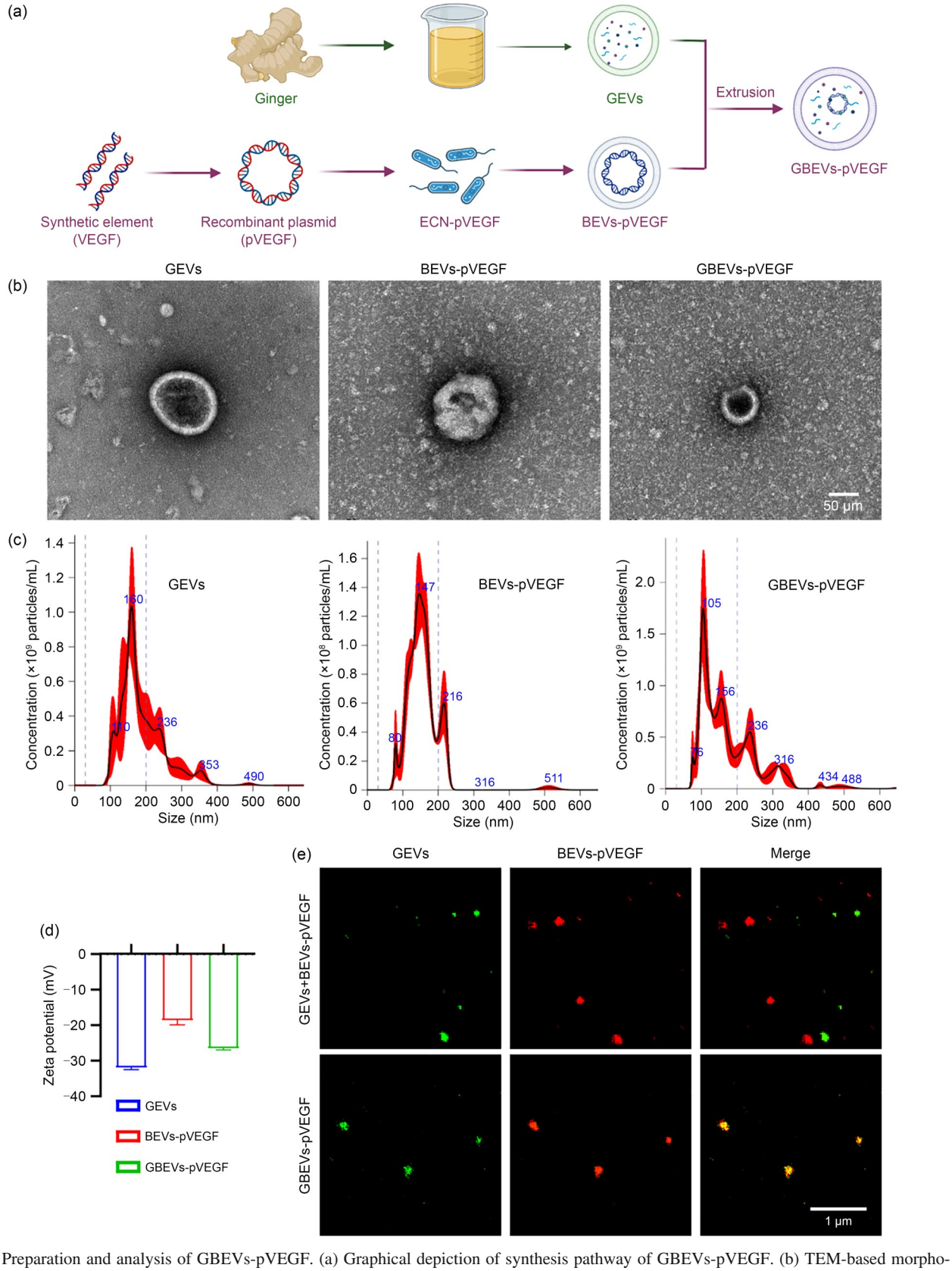

Fig. 1 Preparation and analysis of GBEVs-pVEGF. (a) Graphical depiction of synthesis pathway of GBEVs-pVEGF. (b) TEM-based morphological analysis of GEVs, BEVs-pVEGF, and GBEVs-pVEGF. (c) NTA results of GEVs, BEVs-pVEGF, and GBEVs-pVEGF. (d) Surface zeta potential analysis for GEVs, BEVs-pVEGF, and GBEVs-pVEGF. (e) Confocal fluorescence images of GEVs and BEVs-pVEGF mixture or GBEVs-pVEGF. Data are shown as mean±standard deviation (n=3)

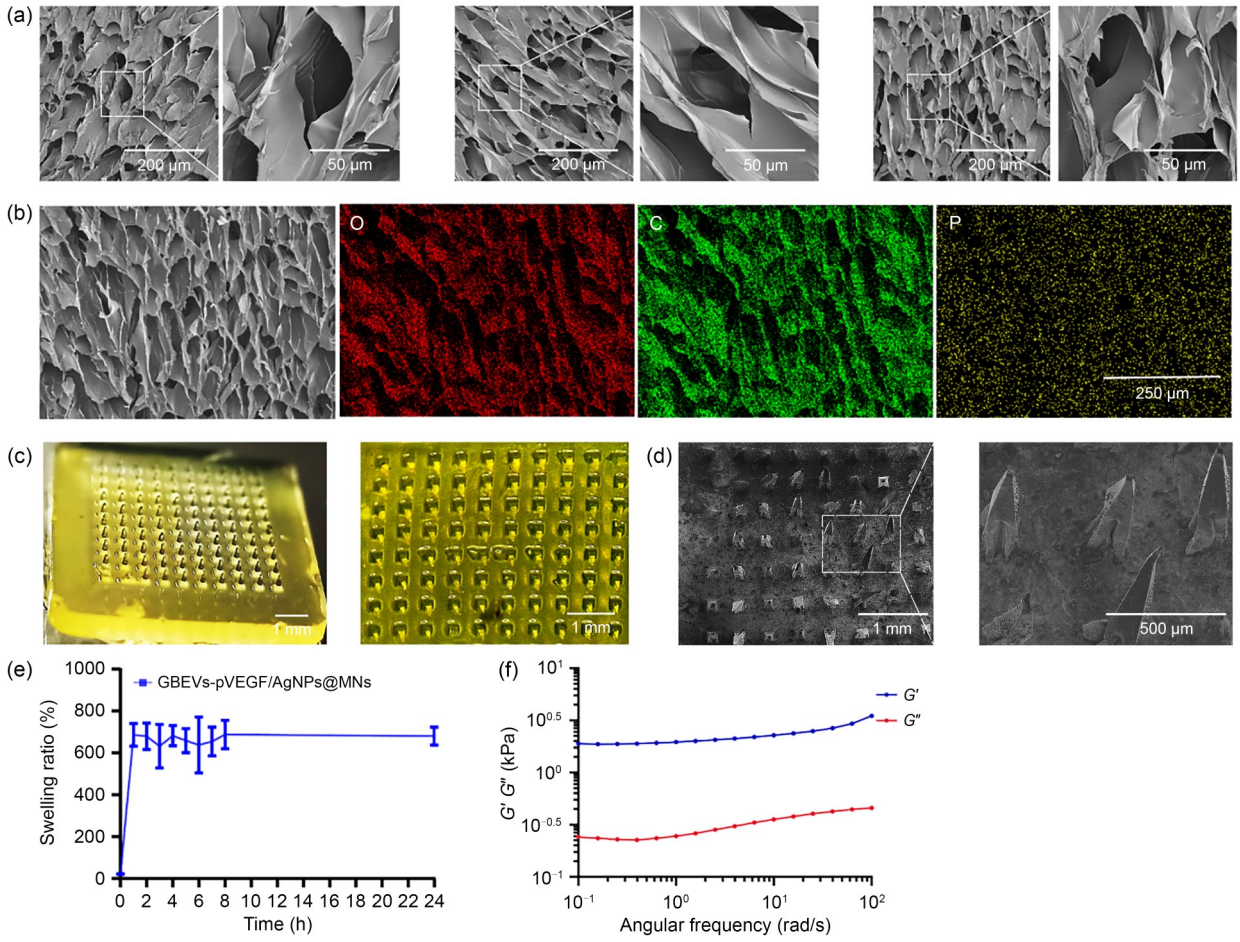

Fig. 2 Characterization of GBEVs-pVEGF/AgNPs@MNs. (a) SEM-based morphological characterization of AlgMA, AgNPs/AlgMA, and GBEVs-pVEGF/AlgMA hydrogels. (b) EDS analysis of GBEVs-pVEGF/AlgMA hydrogels. (c) Optical images of GBEVs-pVEGF/AgNPs@MNs. (d) SEM-based morphological characterization of GBEVs-pVEGF/AgNPs@MNs tips. (e) Swelling behavior of GBEVs-pVEGF/AgNPs@MNs. (f) Rheological analysis of AlgMA hydrogels. Data are shown as mean±standard deviation (n=6)

we performed a 2′,7′-dichlorodihydrofluorescein diacetate (DCFH-DA) test (Fig. 3c), which showed significantly higher ROS levels in RAW 264.7 cells after lipopolysaccharide (LPS) stimulation. However, GBEVs-pVEGF/AgNPs@MNs markedly reduced the intracellular ROS levels in LPS-stimulated cells, restoring them to levels comparable to those in untreated normal cells (Fig. 3f). Similarly, the GEVs/AgNPs@MNs and BEVs-pVEGF/AgNPs@MNs groups exhibited varying degrees of ROS scavenging ability compared with the LPS group. These findings indicate that GBEVs-pVEGF/AgNPs@MNs can effectively reduce intracellular ROS levels through their antioxidant effects.

2.4 Angiogenesis assessment of GBEVs-pVEGF/AgNPs@MNs

To evaluate the effect of GBEVs-pVEGF/AgNPs@MNs on cell migration, scratch assays and Transwell migration assays were conducted. As shown in Figs. 4a and 4d, compared to the control group, GEVs/AgNPs@MNs, BEVs-pVEGF/AgNPs@MNs, and GBEVs-pVEGF/AgNPs@MNs promoted human umbilical vein endothelial cell (HUVEC) migration, with the GBEVs-pVEGF/AgNPs@MNs group demonstrating the most pronounced healing effect (>70%), surpassing that of the BEVs-pVEGF/AgNPs@MNs group. The Transwell migration assay corroborated the above results, thereby highlighting the superior migratory capacity of cells treated with GBEVs-pVEGF/AgNPs@MNs (Figs. 4b and 4e). In addition, GBEVs-pVEGF/AgNPs@MNs could enhance angiogenesis. The tube formation assay results revealed that GBEVs-pVEGF/AgNPs@MNs and BEVs-pVEGF/AgNPs@MNs groups exhibited a higher number of vascular nodes and longer branch lengths than other groups, an effect more pronounced in the GBEVs-pVEGF/AgNPs@MNs group (Figs. 4c, 4f, and 4g). This indicates that the membrane-fused GBEVs-pVEGF exhibited superior pro-migration and tube formation abilities than BEVs-pVEGF alone, likely at least partially due to the synergistic effect of GEVs with BEVs-pVEGF. In conclusion, GBEVs-pVEGF/AgNPs@ MNs significantly enhanced cell migration and angiogenesis in vitro.

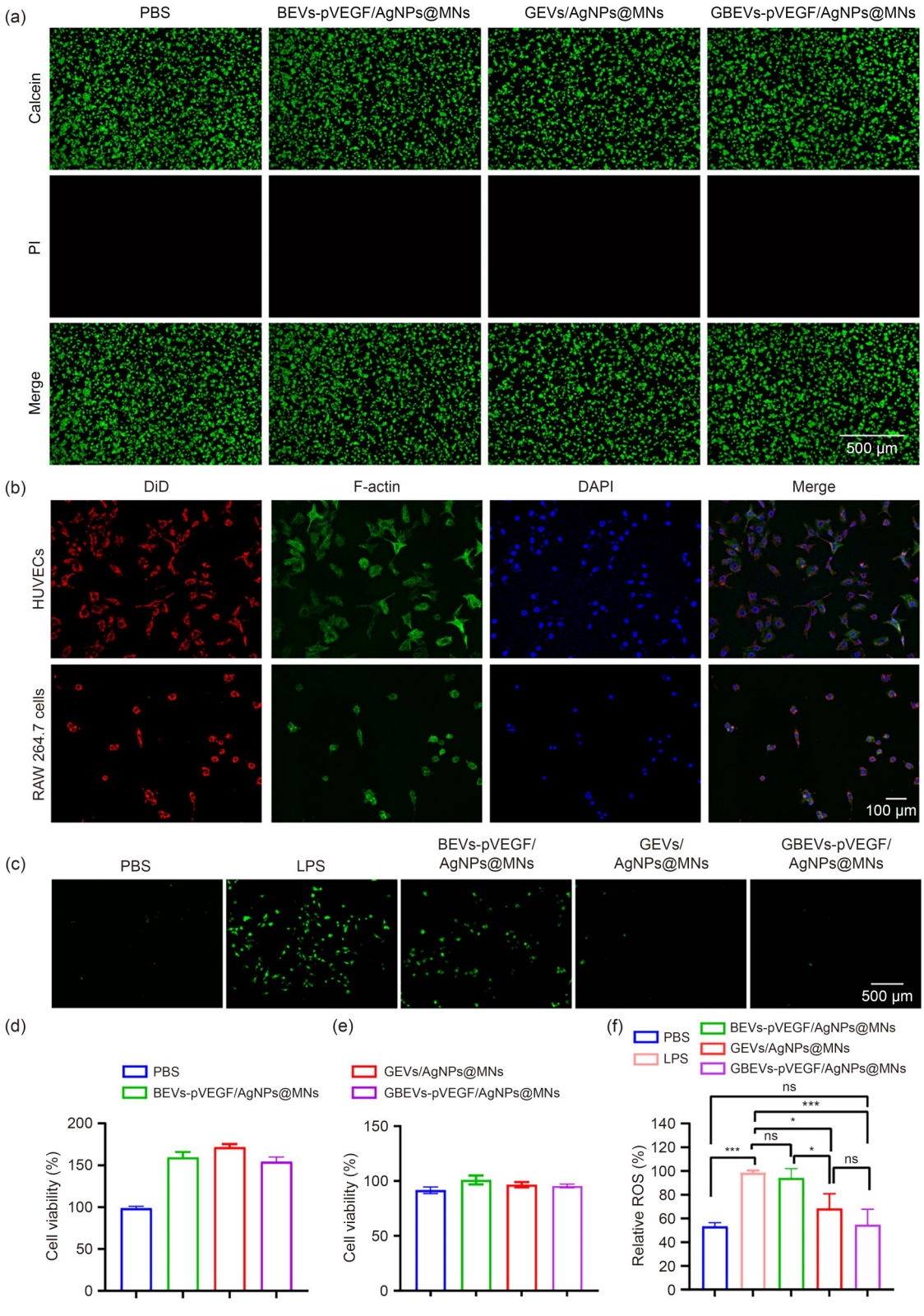

Fig. 3 In vitro evaluation of antioxidant capacity of GBEVs-pVEGF/AgNPs@MNs. (a) Calcein AM/PI staining images of RAW 264.7 cells treated with PBS, BEVs-pVEGF/AgNPs@MNs, GEVs/AgNPs@MNs, and GBEVs-pVEGF/AgNPs@MNs. (b) Confocal fluorescence images of DiD-labeled GBEVs-pVEGF uptake. (c) ROS staining of RAW 264.7 cells using DCFH-DA probe. In vitro cytotoxicity assessment in HUVECs (d) and RAW 264.7 cells (e). (f) Quantitative analysis of relative ROS levels in RAW 264.7 cells. Data are shown as mean±standard deviation (n=3). $^{*}P<0.05$, $^{***}P<0.001$; ns: not significant. PBS: phosphate-buffered saline

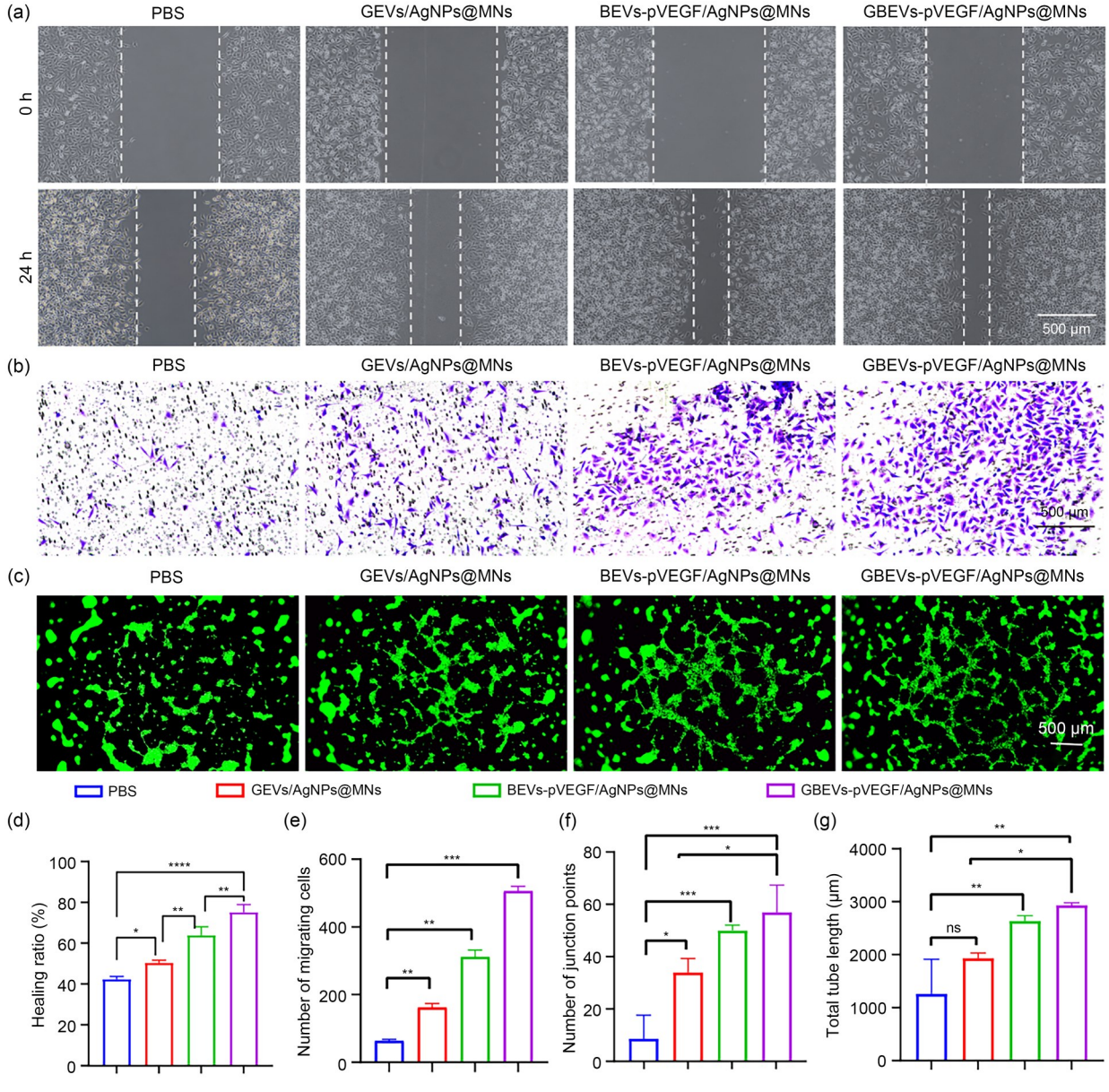

Fig. 4 In vitro assessment of angiogenic potential of GBEVs-pVEGF/AgNPs@MNs. (a) HUVEC migration at 24 h after scratching and quantification of the (d) healing ratio. (b) Transwell migration of HUVECs and quantification of (e) cell migration. (c) Tube formation in HUVECs and quantification of (f) junction points and (g) tube length. Data are shown as mean±standard deviation (n=3). $^{*}P$<0.05, $^{**}P$<0.01, $^{***}P$<0.001, $^{****}P$<0.0001; ns: not significant

2.5 Antibacterial properties of GBEVs-pVEGF/AgNPs@MNs

E. coli and *Staphylococcus aureus* (*S. aureus*), common wound infection pathogens, were used to assess the antibacterial effects of GBEVs-pVEGF/AgNPs@MNs through colony counting and inhibition zone assays [43]. Following treatment with GBEVs-pVEGF/AgNPs@MNs and AgNPs@MNs, *E. coli* growth (>95%) was almost completely inhibited compared to the phosphate-buffered saline (PBS) and GBEVs-pVEGF@MNs groups (Fig. 5a; Fig. S3 in the supplementary information); *S. aureus* (>85%) was similarly suppressed (Fig. 5b; Fig. S3 in the supplementary information), with the inhibitory effects in both experimental groups being nearly identical. Consistent with these findings, the inhibition zone assay for both bacteria revealed that the diameters of the inhibition zones (DIZs) produced by GBEVs-pVEGF/AgNPs@MNs and AgNPs@MNs were similar but significantly larger than those of PBS and GBEVs-pVEGF@MNs (Fig. 5c; Fig. S4 in the supplementary information). The above results indicate that GBEVs-pVEGF/AgNPs@MNs effectively release AgNPs and demonstrate robust antibacterial properties against *E. coli* and *S. aureus*. The comparable antibacterial efficacy to AgNPs@MNs implies that the

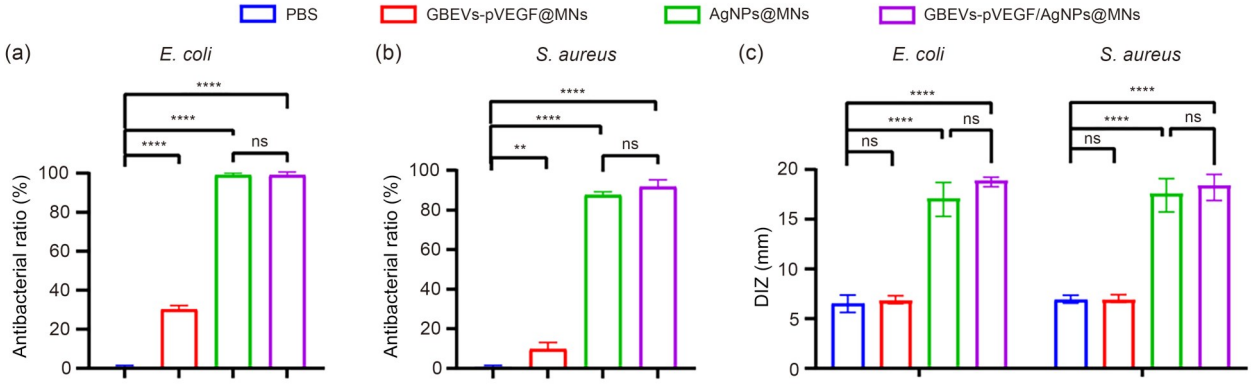

Fig. 5 In vitro evaluation of antimicrobial activity of GBEVs-pVEGF/AgNPs@MNs. Quantitative analysis of the antibacterial ratio of *E. coli* (a) and *S. aureus* (b). (c) Quantitative analysis of DIZs for *E. coli* and *S. aureus*. Data are shown as mean±standard deviation (n=3). $^{**}P<0.01$, $^{****}P<0.0001$; ns: not significant

inclusion of GBEVs-pVEGF does not compromise the antimicrobial potency of AgNPs.

2.6 Assessment of diabetic wound healing by GBEVs-pVEGF/AgNPs@MNs

To further validate the therapeutic efficacy of GBEVs-pVEGF/AgNPs@MNs in vivo, a full-thickness skin wound model was established in streptozotocin (STZ)-induced diabetic mice. STZ induces diabetes by selectively destroying insulin-producing β cells in the pancreas, leading to hyperglycemia and metabolic alterations that resemble key features of diabetes. Although the STZ-induced diabetic mouse model has certain limitations in mimicking the physiological and pathological characteristics of diabetic wounds in clinical patients, it is a common experimental model in diabetic wound research [9, 44]. After producing a 10-mm diameter wound on the back of diabetic mice using a skin punch, the wound was subsequently treated with AgNPs@MNs, BEVs-pVEGF/AgNPs@MNs, GEVs/AgNPs@MNs, and GBEVs-pVEGF/AgNPs@MNs, using Tegaderm dressing as control (Fig. 6a).

Figures 6b and 6c illustrate the photographs of wounds and their healing trajectories across various treatment groups at distinct time points over a 14-d period. On Day 7, the GBEVs-pVEGF/AgNPs@MNs group demonstrated a pronounced diminution in the wound area, whereas the GEVs/AgNPs@MNs, BEVs-pVEGF/AgNPs@MNs, and AgNPs@MNs groups exhibited varying degrees of healing efficacy relative to the control group (Fig. 6d). On Day 14, the wound in the GBEVs-pVEGF/AgNPs@MNs group showed near-complete healing. In contrast, the other groups retained varying degrees of residual wound areas (Fig. 6d). Collectively, these findings indicate that the synergistic interplay between the antioxidant and angiogenic attributes of GBEVs-pVEGF and the intrinsic antimicrobial properties of AgNPs and MNs significantly reduces the healing time of diabetic wounds.

Histological analysis using hematoxylin and eosin (H&E) staining and Masson's trichrome staining was conducted to assess the wound healing process and the quality of the newly formed skin in diabetic wounds. During the inflammatory stage of diabetic wound repair, excessive intracellular ROS levels not only promote the recruitment of inflammatory cells and fibroblasts but also lead to tissue structure disruption, thereby exacerbating wound healing difficulties by triggering inflammation [9]. As shown in Fig. 6e, the diabetic wounds in the control group on Day 7 exhibited disorganized tissue structure, incomplete epithelial coverage, and extensive inflammatory cell infiltration, potentially prolonging the inflammatory phase and hindering wound healing. In contrast, the hydrogel MN groups demonstrated a reduction in inflammatory cell infiltration and increased fibroblast migration. Among them, the GBEVs-pVEGF/AgNPs@MNs group exhibited granulation tissue formation and a reduction in inflammatory cell infiltration on Day 7. On Day 14, the GBEVs-pVEGF/AgNPs@MNs group exhibited complete epithelial coverage, a highly organized tissue structure, and newly formed blood vessels (Fig. 6f).

2.7 Collagen deposition and angiogenesis analysis in vivo

Subsequently, Masson's trichrome staining was employed to evaluate collagen deposition across treatment groups. In the remodeling phase, fibroblasts infiltrate the wound area and synthesize collagen, which promotes the development of the extracellular matrix and expedites wound healing [45]. On Day 7, varying levels of collagen deposition were observed among hydrogel MN groups, with the most pronounced collagen deposition found in the GBEVs-pVEGF/AgNPs@MNs group, while the control group exhibited the least (Fig. 7a). On Day 14, the GBEVs-pVEGF/AgNPs@MNs group exhibited maximal collagen deposition, whereas the GEVs/AgNPs@MNs group showed less (Fig. 7b). These

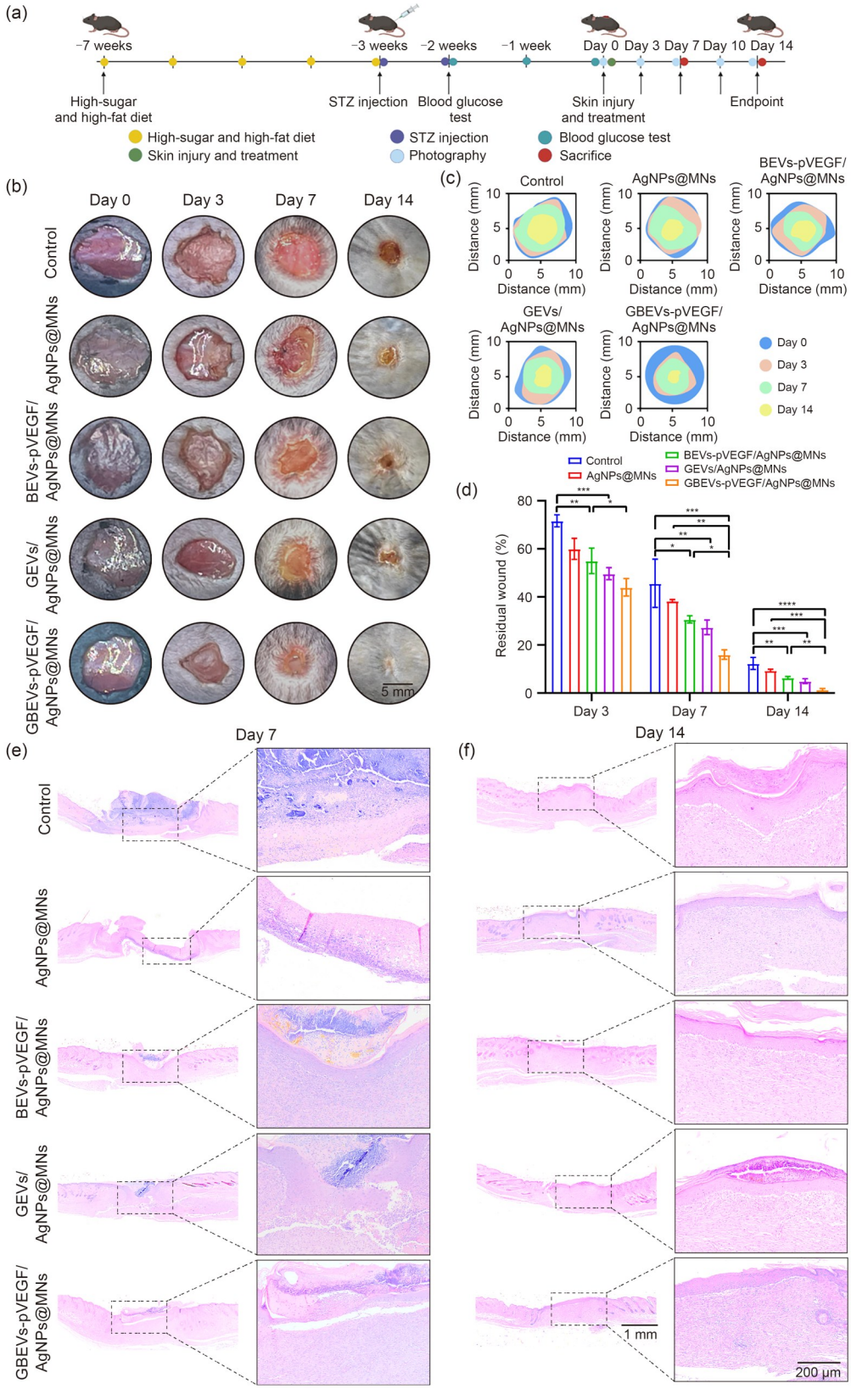

Fig. 6 In vivo GBEVs-pVEGF/AgNPs@MNs treatment accelerates diabetic wound healing. (a) Experimental scheme for diabetic full-thickness wound management in mice. (b) Representative wound healing images (Days 0–14). (c) Diabetic wound healing traces. (d) Percentage of residual wounds. H&E staining of diabetic wounds on Days 7 (e) and 14 (f). Data are shown as mean±standard deviation (n=6). $^{*}P<0.05$, $^{**}P<0.01$, $^{***}P<0.001$, and $^{****}P<0.0001$

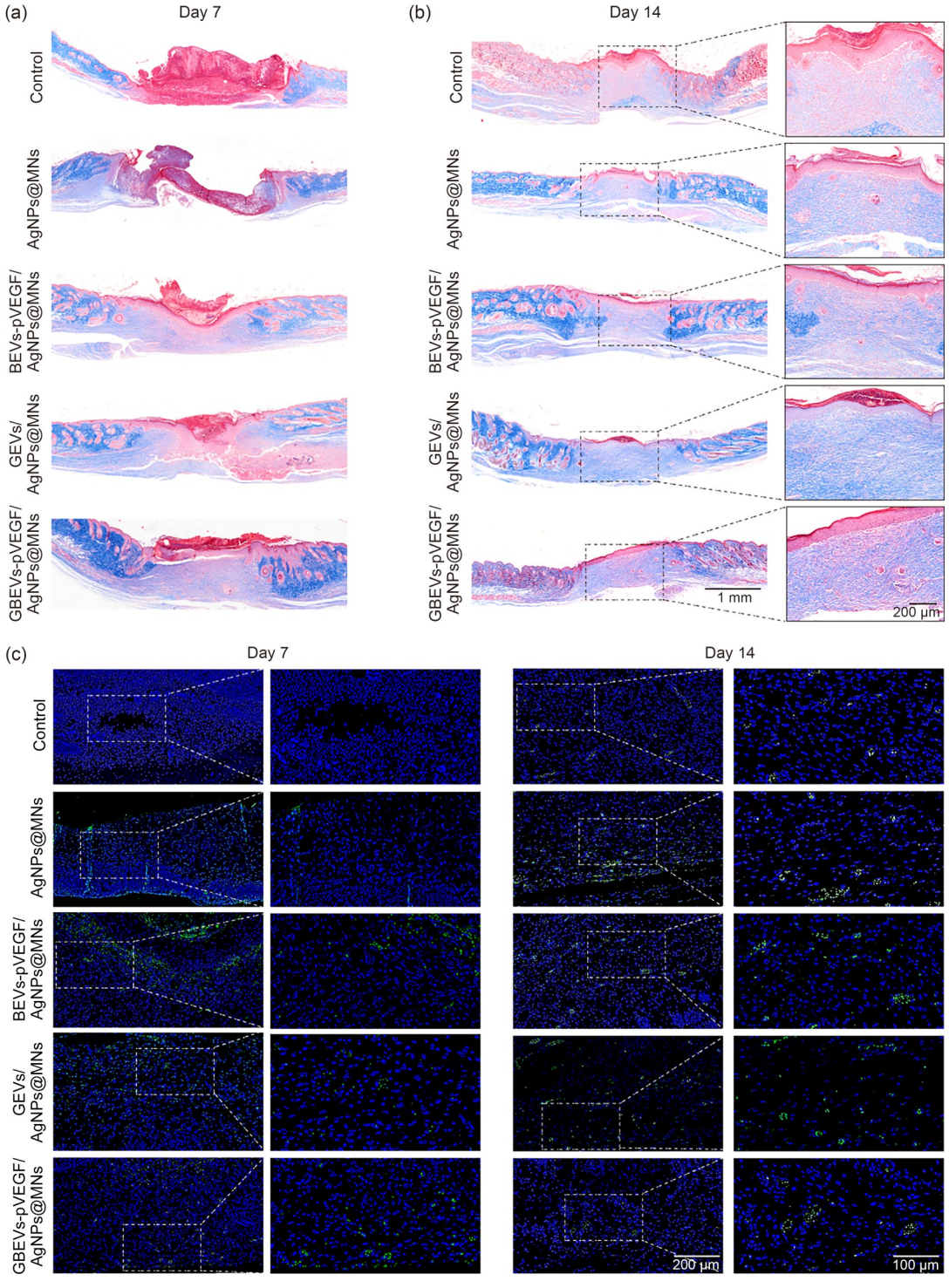

Fig. 7 In vivo assessment of GBEVs-pVEGF/AgNPs@MNs in enhancing collagen deposition and angiogenesis. Masson's trichrome staining of diabetic wounds on Days 7 (a) and 14 (b). (c) CD31 immunofluorescence images of wound (green immunofluorescence indicates the endothelial cells marker CD31, while blue fluorescence shows 4′,6-diamidino-2-phenylindole (DAPI)-stained nuclei)

findings indicate that GBEVs-pVEGF/AgNPs@MNs can significantly enhance diabetic wound healing by promoting accelerated collagen deposition.

As shown in Fig. 7c, immunofluorescence staining was used to evaluate the differences in angiogenesis among treatment groups. During wound healing, the proliferative phase is characterized by a significant increase in angiogenesis, with most of these blood vessels being immature and having small lumens. CD31 immunofluorescence staining showed the highest density of newly formed blood vessels in the

GBEVs-pVEGF/AgNPs@MNs group on Day 7, with the GEVs/AgNPs@MNs and BEVs-pVEGF/AgNPs@MNs groups showing relatively low densities. In the remodeling phase, during which new blood vessels matured and developed into stable tubular structures, compared with the other groups, GBEVs-pVEGF/AgNPs@MNs had a higher number of blood vessels with well-defined lumen structures on Day 14. These results indicate that GBEVs-pVEGF/AgNPs@MNs possess a superior angiogenic potential to that of BEVs-pVEGF/AgNPs@MNs, suggesting that GEVs contribute to enhanced angiogenesis.

3 Conclusions

In summary, we have developed a dual-component, multifunctional hydrogel MNs (GBEVs-pVEGF/AgNPs@MNs) that provide sustained drug delivery to the wound site, effectively mitigating oxidative stress, exerting antibacterial activity, and promoting angiogenesis. Considering that diabetic wound healing is a continuous and dynamic process, the GBEVs-pVEGF within the MN base significantly reduce ROS levels and enhance the migration and tube formation of HUVECs. Additionally, the AgNPs in the base layer alleviate persistent bacterial infections during the wound-healing process. In diabetic mice, GBEVs-pVEGF/AgNPs@MNs facilitate angiogenesis and collagen deposition through localized drug delivery, thereby accelerating wound closure.

The current research predominantly focuses on cellular and diabetic mouse wound models, which have preliminarily demonstrated the efficacy of GBEVs-pVEGF/AgNPs@MNs. However, the pathological characteristics of chronic diabetic wounds in clinical settings are highly complex and heterogeneous, and the existing models fail to fully capture these features. Therefore, future studies will incorporate standard clinical treatments as control groups and utilize models that more closely mimic the physiological and pathological characteristics of human diabetic wounds to further evaluate the therapeutic effects of GBEVs-pVEGF/AgNPs@MNs in accelerating wound healing, thereby providing valuable insights for the clinical management of diabetic wounds.

4 Materials and methods

4.1 Synthesis of shuttle plasmids

To construct the shuttle plasmid pVEGF, a 20 μL reaction mixture consisting of 1 μL of pEGFP-N1 plasmid (with homologous sequences at both ends for cloning), 2 μL of the VEGF fragment (from polymerase chain reaction (PCR) or gene synthesis), 10 μL of one-step cloning enzyme mix, and ddH_2O was prepared. The mixture was incubated at 50 °C for 20 min to facilitate ligation of the VEGF plasmid into the pEGFP-N1 vector.

4.2 Generation of engineered probiotics

The probiotic strain was grown for 10 h in 5 mL of Luria–Bertani (LB) medium, and then transferred to 100 mL of LB medium for 3 h more. When the optical density at 600 nm reached 0.6, the culture was harvested and cooled in an ice bath for 30 min. The probiotics were centrifuged at 7500 r/min for 10 min at 4 °C, followed by the removal of the supernatant. A second centrifugation was performed under identical conditions. The pellet was then resuspended in a 0.1 mol/L $CaCl_2$ solution containing 0.1 g/mL glycerol to produce calcium-competent probiotics. Then, the shuttle plasmid pVEGF was introduced into competent probiotics by adding the plasmid to the resuspended bacterial solution. The mixture was placed on ice for 30 min, followed by a 120-s heat shock at 42 °C and cooling on ice for 10 min. After adding 1800 μL of LB medium, the culture was incubated at 37 °C for 2 h. The bacterial suspension was centrifuged to remove the supernatant and then resuspended. Finally, 200 μL of the resuspended solution was plated, inverted, and incubated at 37 °C to obtain probiotics carrying pVEGF.

4.3 Strain cultivation and isolation of BEVs-pVEGF

The engineered probiotics were aerobically cultured in LB medium at 37 °C and 220 r/min for 12 h to generate a primary culture. Subsequently, 1 mL of the primary culture was inoculated into 100 mL of LB medium and incubated under the same conditions to generate a secondary culture. The obtained culture was first subjected to low-speed centrifugation at 12 500*g* for 30 min to remove bacterial cells and metabolic waste products. Then, the supernatant was filtered through a 0.22-μm sterile filter (Millipore, USA), ultracentrifuged at 150 000*g* for 3 h, and the pellet was suspended to obtain BEVs-pVEGF. All BEVs-pVEGF isolation steps were performed at 4 °C.

4.4 Isolation and purification of GEVs

Fresh ginger was peeled and juiced, followed by initial filtration with gauze. The supernatant underwent differential centrifugation (3000*g* for 30 min, followed by 8000, 10 000, and 13 000*g* for 1 h each), and was then filtered through a 0.22-μm sterile filter. The pellets were subsequently collected by ultracentrifugation at 150 000*g* for 3 h. The resuspended pellets were further purified using a sucrose density gradient to obtain GEVs. All GEV isolation steps were performed at 4 °C.

4.5 Preparation and characterization of GBEVs-pVEGF

During the preparation of GBEVs-pVEGF, GEVs and BEVs-pVEGF were initially concentrated to achieve identical volumes with nearly equivalent particle counts, based on a predetermined volume ratio (GEVs:BEVs-pVEGF=1:10). Subsequently, equal volumes of GEVs (1×10^{10} particles/mL) and BEVs-pVEGF (1×10^{10} particles/mL) were mixed and subjected to ultrasonication for 10 min at 4 °C. The mixture was then processed through an Avanti mini-extruder (Avanti Polar Lipids, USA) equipped with polycarbonate membranes of 100, 200, and 400 nm pore sizes to ensure uniform particle size distribution. The morphology, particle size, and zeta potential of the resulting GBEVs-pVEGF were characterized using transmission electron microscopy (TEM; Hitachi HT7700, Japan), nanoparticle tracking analysis (NTA; NanoSight NS300, Malvern Panalytical, UK), and dynamic light scattering (Zetasizer nano ZS90; Malvern Panalytical, UK), respectively.

4.6 Membrane fusion assessment of GBEVs-pVEGF

To confirm the successful fusion of GEVs and BEVs-pVEGF, GEVs were labeled with 3,3′-dioctadecyloxacarbocyanine perchlorate (DiO) (excitation/emission: 484 nm/501 nm; Beyotime, China) and BEVs-pVEGF with 1,1′-dioctadecyl-3,3,3′,3′-tetramethylindocarbocyanine perchlorate (DiI) (excitation/emission: 549 nm/565 nm; Beyotime). The excess dye was then removed by 150 000*g* centrifugation for 90 min. The fused GBEVs-pVEGF and the GEVs-BEVs-pVEGF mixture were observed using a confocal fluorescence microscope (LSM-710, Zeiss, Germany).

4.7 Synthesis of AlgMA, AgNPs/AlgMA, and GBEVs-pVEGF/AlgMA hydrogels

A total of 0.36 g of AlgMA (Engineering for Life, China) was dissolved in 6 mL of deionized water and incubated at 37 °C for 30 min. GBEVs-pVEGF and AgNPs (Aladdin, China) were added to 1×10^{10} particles/mL and 200 μg/mL, respectively. Then, 2.5 g/L photoinitiator lithium phenyl (2,4,6-trimethylbenzoyl) phosphinate (LAP; Engineering for Life) was added, and the mixture was incubated and exposed to 450 nm ultraviolet (UV) light to form AlgMA, AgNPs/AlgMA, and GBEVs-pVEGF/AlgMA hydrogels. Subsequently, the hydrogels were freeze-dried, and their pore size and elemental composition were analyzed via an SEM (GeminiSEM 300, Zeiss) and an EDS (AztecLive Ultim-Max 100, Oxford Instruments, UK). Next, the rheological properties of AlgMA hydrogels were analyzed at 37 °C using a rheometer (HR-20, TA Instruments, USA). Measurements were performed on a 20-mm plate with a 1-mm gap, assessing G' and G'' through a time sweep at 1% strain and 10 rad/s.

4.8 Fabrication of GBEVs-pVEGF/AgNPs@MNs

Hydrogel MNs comprise a tip layer (GBEVs-pVEGF/AlgMA) and a base layer (AgNPs/AlgMA). Initially, 100 μL of GBEVs-pVEGF/AlgMA hydrogel was added to the MN mold (EFL-MMN-800, Engineering for Life) and subjected to vacuum degassing to remove air bubbles. Then, the MN mold was thermally concentrated at 37 °C for 4 h to form the MN tips. Then, the AgNPs/AlgMA hydrogel was added to form the base layer and concentrated under the same conditions. After photopolymerization and drying for 48 h, the mold was removed, and morphology was assessed via SEM after freeze-drying.

4.9 Swelling test of GBEVs-pVEGF/AgNPs@MNs

After freeze-drying GBEVs-pVEGF/AgNPs@MNs, the dry weight (W_0) was recorded. The samples were immersed in PBS at 37 °C, and their swelling weight (W_1) was measured at intervals, with excess moisture blotted off using absorbent paper before weighing. The swelling ratio was calculated as follows:

$$r_{\text{Swelling}}=(W_1 - W_0)/W_0 \times 100\%. \quad (1)$$

4.10 Biocompatibility assessment of GBEVs-pVEGF/AgNPs@MNs

HUVECs and RAW 264.7 cells were maintained in Dulbecco's modified Eagle medium (DMEM) (Gibco, USA) with 0.1 g/mL fetal bovine serum (FBS; Sigma, USA) and 10 g/L penicillin-streptomycin (Beyotime) at 37 ℃ in a 5% CO_2 incubator. Cells were inoculated at concentrations of 10^3 or 10^5 per well in 96- or 12-well plates. After 24 h, the medium was replaced with extracts containing BEVs-pVEGF/AgNPs@MNs, GEVs/AgNPs@MNs, and GBEVs-pVEGF/AgNPs@MNs, using PBS as a control. After 24 h, cell viability was assessed using the CCK-8 (Beyotime) and the Calcein AM/PI staining kit (Beyotime).

4.11 Internalization capacity of GBEVs-pVEGF

To evaluate GBEVs-pVEGF internalization, HUVECs and RAW 264.7 cells were cultured overnight in 12-well plates and incubated with 1,1′-dioctadecyl-3,3,3′,3′-tetramethylindodicarbocyanine, 4-chlorobenzenesulfonate salt (DiD)-labeled GBEVs-pVEGF for 6 h (excitation/emission: 644 nm/665 nm; Beyotime). After incubation, noninternalized EVs

were removed by washing with PBS. After fixation with 40 g/L paraformaldehyde (Servicebio, China) for 15 min, the cytoskeleton was stained with F-actin (Solarbio, China) and the nucleus with DAPI (Solarbio). Finally, fluorescence images were captured by confocal fluorescence microscopy.

4.12 In vitro antioxidant activity assessment

To evaluate the effectiveness of hydrogel MNs in mitigating LPS-induced oxidative stress, RAW 264.7 cells were seeded in 96-well plates and treated with LPS (200 ng/mL) for 24 h to induce oxidative stress. The cells were then exposed to a culture medium containing different hydrogel MN soaking solutions, and ROS scavenging was measured using the ROS assay kit (Beyotime). Finally, the fluorescence images were captured, and their intensity was quantified to evaluate the ROS scavenging efficiency.

4.13 In vitro cell scratch test

The impact of GBEVs-pVEGF/AgNPs@MNs on wound healing was evaluated using HUVECs. HUVECs were plated in 6-well plates and allowed to establish a confluent monolayer. Following a 24-h starvation period in a medium devoid of FBS, a vertical scratch was introduced on the cellular monolayer utilizing a 100-μL pipette tip. Subsequently, the culture medium was exchanged for another supplemented with various hydrogel extracts, and the cells were cultured for an additional 24 h. Images were captured at 0 and 24 h, and the nonhealed areas were quantified.

4.14 In vitro cell Transwell migration assay

The effect of GBEVs-pVEGF/AgNPs@MNs on cell migration was assessed using a Transwell assay. HUVECs in serum-free medium were plated in the apical chamber of 12-well Transwell inserts. To facilitate cell migration, the basal chamber was filled with medium (10 g/L FBS) containing hydrogel extracts. After 24 h, the cells on the lower membrane surface were fixed with 40 g/L paraformaldehyde for 30 min, stained with crystal violet staining solution (Beyotime), and observed under a microscope. Migrated cells were counted for statistical analysis.

4.15 In vitro tube formation assessment

HUVECs were seeded onto a 96-well plate coated with Matrigel (50 μL) and cultured in medium containing hydrogel MN exudates for 6 h. Next, cells were stained for 30 min following the instructions of the Calcein AM/PI staining kit (Beyotime). Fluorescent images were captured, and the number of vascular junction points and total vessel length were analyzed.

4.16 In vitro antibacterial activity assessment

The antibacterial activity of MN samples against *E. coli* and *S. aureus* was evaluated using colony counting and the inhibition zone assay. A bacterial suspension with a density of 1×10^8 CFU/mL (CFU: colony-forming unit) was incubated in LB liquid medium containing different MN samples at 37 °C for 12 h. The bacterial suspension was then diluted 1000-fold, and the diluted sample was inoculated onto the surface of LB agar plates using glass beads (Sangon Biotech, China). Then, the plates were incubated at 37 °C in an inverted position for 24 h. Colony counts were documented, and the antibacterial efficacy was determined as follows:

$$E_{\text{Antibacterial}} = (C_C - C_E)/C_C \times 100\%, \quad (2)$$

where C_C and C_E represent the control colony count and experimental colony count, respectively.

The antibacterial potency of MN samples was further evaluated with the inhibition zone assay. Initially, *E. coli* and *S. aureus* were cultured up to a concentration of 1×10^8 CFU/mL. These bacterial suspensions were then inoculated onto LB agar plates. Subsequently, the distal end (the wider part) of a 100-μL pipette was used to create cylindrical wells 4 mm deep in the agar plates. The soaking solutions of various MNs were added to these wells. Following incubation at 37 °C for 24 h in an upright orientation, the antibacterial activity was quantified by measuring DIZ.

4.17 In vivo wound healing

Six-week-old male C57BL/6 mice were purchased from Changzhou Cavens Experimental Animal Co., Ltd., China. A type 2 diabetes full-thickness wound model was established in those mice. Mice were fed a high-fat, high-sugar diet for four weeks to induce insulin resistance. Subsequently, they were administered STZ (10 mg/kg) via intraperitoneal injection for one week. The type 2 diabetes model was considered successfully established when blood glucose levels stayed >16.7 mmol/L for two weeks. After diabetes induction, mice were anesthetized, and a 10-mm full-thickness wound was created on the dorsal surface using a skin punch tool. Next, wounds were treated with AgNPs@MNs, BEVs-pVEGF/AgNPs@MNs, GEVs/AgNPs@MNs, and GBEVs-pVEGF/AgNPs@MNs, using Tegaderm dressings (1626W, Tegaderm™, USA) as control. Wound images were acquired, and wound areas were quantified at 0, 3, 7, and 14 d. At the end of the study, histological examinations were performed posteuthanasia to assess healing.

4.18 Histological staining

Wound tissues collected on Days 7 and 14 were subjected to H&E staining and Masson's trichrome staining for histological analysis. First, tissue sections were fixed in 40 g/L

paraformaldehyde, followed by paraffin embedding and sectioning into 5-μm-thick slices, before staining. Images were captured using a microscope (VS200, Olympus, Japan).

4.19 Immunofluorescence staining

For immunofluorescence staining, the samples were incubated overnight at 4 °C with primary anti-CD31 antibodies (1: 500, ab222783; Abcam, UK), followed by incubation with secondary fluorescein isothiocyanate (FITC)-conjugated antibodies (1:1000; Proteintech, USA) at 37 °C for 1 h. Subsequently, samples were mounted using a DAPI-containing mounting medium (Servicebio). Finally, images were captured using a microscope.

4.20 Statistical analysis

Statistical analyses were conducted using GraphPad Prism 10.2.0 (GraphPad Software, USA). Results are shown as mean±standard deviation, and group comparisons were performed using one-way analysis of variance (ANOVA) with Tukey's test. Significance was defined as $^{*}P<0.05$, $^{**}P<0.01$, $^{***}P<0.001$, and $^{****}P<0.0001$.

Supplementary Information The online version contains supplementary material available at https://doi.org/10.1631/bdm.2500061.

Acknowledgements The authors acknowledge the financial support from the National Natural Science Foundation of China (No. 82472444).

Author contributions YS: writing—original draft, methodology, investigation, formal analysis, data curation, and conceptualization. QRZ: writing—original draft, methodology, and data curation. SHS: investigation and conceptualization. HJY: formal analysis and data curation. LB: methodology, investigation, and formal analysis. ZG: writing—review & editing, investigation, and formal analysis. JW: validation and formal analysis. KX: validation, supervision, and conceptualization. XC: writing—review & editing, supervision, and resources. YYJ: writing—review & editing, supervision, and resources. GCW: writing—review & editing, supervision, and resources. JCS: writing—review & editing, supervision, resources, project administration, funding acquisition, and conceptualization.

Declarations

Conflict of interest The authors declare that they have no conflict of interest.

Ethical approval All experimental procedures were performed in accordance with the Guide for the Care and Use of Laboratory Animals of the National Research Council. All animal-related surgical interventions were authorized by the Animal Ethics Committee of the Institute of Translational Medicine, Shanghai University, under protocol number YS2023-041. These procedures adhered to the standards for the care and use of laboratory animals detailed in NIH Publication No. 8023 (revised 1978) to ensure ethical and humane treatment.

Data availability The data that support the findings of this study are available from the corresponding authors upon reasonable request.

References

1. McDermott K, Fang M, Boulton AJM et al (2023) Etiology, epidemiology, and disparities in the burden of diabetic foot ulcers. Diabetes Care 46(1):209–221. https://doi.org/10.2337/dci22-0043
2. Sun H, Saeedi P, Karuranga S et al (2022) IDF Diabetes Atlas: global, regional and country-level diabetes prevalence estimates for 2021 and projections for 2045. Diabetes Res Clin Pract 183: 109119. https://doi.org/10.1016/j.diabres.2021.109119
3. Wang YL, Lin QS, Zhang H et al (2023) M2 macrophage-derived exosomes promote diabetic fracture healing by acting as an immunomodulator. Bioact Mater 28:273–283. https://doi.org/10.1016/j.bioactmat.2023.05.018
4. Liu WS, Gao R, Yang CF et al (2022) ECM-mimetic immunomodulatory hydrogel for methicillin-resistant *Staphylococcus aureus*-infected chronic skin wound healing. Sci Adv 8(27): eabn7006. https://doi.org/10.1126/sciadv.abn7006
5. Zhang T, Sheng SH, Cai WH et al (2024) 3-D bioprinted human-derived skin organoids accelerate full-thickness skin defects repair. Bioact Mater 42:257–269. https://doi.org/10.1016/j.bioactmat.2024.08.036
6. West XZ, Malinin NL, Merkulova AA et al (2010) Oxidative stress induces angiogenesis by activating TLR2 with novel endogenous ligands. Nature 467(7318):972–976. https://doi.org/10.1038/nature09421
7. Bryan N, Ahswin H, Smart N et al (2012) Reactive oxygen species (ROS)—a family of fate deciding molecules pivotal in constructive inflammation and wound healing. Eur Cell Mater 24: 249–265. https://doi.org/10.22203/ecm.v024a18
8. Lei H, Fan DD (2022) A combination therapy using electrical stimulation and adaptive, conductive hydrogels loaded with self-assembled nanogels incorporating short interfering RNA promotes the repair of diabetic chronic wounds. Adv Sci 9(30): 2201425. https://doi.org/10.1002/advs.202201425
9. Liang Z, Luo JL, Liu SM et al (2023) Injectable, antibacterial, ROS scavenging and pro-angiogenic hydrogel adhesives promote chronic wound healing in diabetes via synergistic release of NMN and Mg^{2+}. Chem Eng J 475:146092. https://doi.org/10.1016/j.cej.2023.146092
10. Liu WS, Ouyang WB, Zhang C et al (2020) Synthetic polymeric antibacterial hydrogel for methicillin-resistant *Staphylococcus aureus*-infected wound healing: nanoantimicrobial self-assembly, drug- and cytokine-free strategy. ACS Nano 14(10):12905–12917. https://doi.org/10.1021/acsnano.0c03855
11. Eming SA, Martin P, Tomic-Canic M (2014) Wound repair and regeneration: mechanisms, signaling, and translation. Sci Transl Med 6(265):265sr6. https://doi.org/10.1126/scitranslmed.3009337
12. van Niel G, D'Angelo G, Raposo G (2018) Shedding light on the cell biology of extracellular vesicles. Nat Rev Mol Cell Biol 19(4):213–228. https://doi.org/10.1038/nrm.2017.125
13. Liu H, Geng Z, Su JC (2022) Engineered mammalian and bacterial extracellular vesicles as promising nanocarriers for targeted therapy. Extracell Vesicles Circ Nucleic Acids 3(2):63–86. https://doi.org/10.20517/evcna.2022.04
14. Kalluri R, LeBleu VS (2020) The biology, function, and biomedical applications of exosomes. Science 367(6478):eaau6977. https://doi.org/10.1126/science.aau6977
15. Ren XX, Xu RX, Xu CJ et al (2024) Harnessing exosomes for targeted therapy: strategy and application. Biomater Transl 5(1):

46–58.
https://doi.org/10.12336/biomatertransl.2024.01.005
16. Zeng ZL, Xie H (2022) Mesenchymal stem cell-derived extracellular vesicles: a possible therapeutic strategy for orthopaedic diseases: a narrative review. Biomater Transl 3(3):175–187.
https://doi.org/10.12336/biomatertransl.2022.03.002
17. Sall IM, Flaviu TA (2023) Plant and mammalian-derived extracellular vesicles: a new therapeutic approach for the future. Front Bioeng Biotechnol 11:1215650.
https://doi.org/10.3389/fbioe.2023.1215650
18. Liu H, Li MM, Zhang T et al (2022) Engineered bacterial extracellular vesicles for osteoporosis therapy. Chem Eng J 450:138309.
https://doi.org/10.1016/j.cej.2022.138309
19. Han RN, Wu Y, Han YF et al (2024) Engineered plant extracellular vesicles for autoimmune diseases therapy. Nano Res 17(4):2857–2873.
https://doi.org/10.1007/s12274-023-6112-1
20. Feng JJ, Xiu Q, Huang YY et al (2023) Plant-derived vesicle-like nanoparticles as promising biotherapeutic tools: present and future. Adv Mater 35(24):2207826.
https://doi.org/10.1002/adma.202207826
21. Huang RF, Jia B, Su DD et al (2023) Plant exosomes fused with engineered mesenchymal stem cell-derived nanovesicles for synergistic therapy of autoimmune skin disorders. J Extracell Vesicles 12(10):e12361.
https://doi.org/10.1002/jev2.12361
22. Mahmud MR, Akter S, Tamanna SK et al (2022) Impact of gut microbiome on skin health: gut-skin axis observed through the lenses of therapeutics and skin diseases. Gut Microbes 14(1):e2096995.
https://doi.org/10.1080/19490976.2022.2096995
23. Zhang YF, Gu YY, Ren HH et al (2020) Gut microbiome-related effects of berberine and probiotics on type 2 diabetes (the PREMOTE study). Nat Commun 11(1):5015.
https://doi.org/10.1038/s41467-020-18414-8
24. Wang SJ, Ren HH, Zhong HZ et al (2022) Combined berberine and probiotic treatment as an effective regimen for improving postprandial hyperlipidemia in type 2 diabetes patients: a double blinded placebo controlled randomized study. Gut Microbes 14(1):e2003176.
https://doi.org/10.1080/19490976.2021.2003176
25. Liu H, Zhang Q, Wang SC et al (2022) Bacterial extracellular vesicles as bioactive nanocarriers for drug delivery: advances and perspectives. Bioact Mater 14:169–181.
https://doi.org/10.1016/j.bioactmat.2021.12.006
26. Liu H, Zhang H, Wang SC et al (2023) Bone-targeted bioengineered bacterial extracellular vesicles delivering siRNA to ameliorate osteoporosis. Compos Part B Eng 255:110610.
https://doi.org/10.1016/j.compositesb.2023.110610
27. Liu H, Song PR, Zhang H et al (2024) Synthetic biology-based bacterial extracellular vesicles displaying BMP-2 and CXCR4 to ameliorate osteoporosis. J Extracell Vesicles 13(4):e12429.
https://doi.org/10.1002/jev2.12429
28. Cheng KM, Zhao RF, Li Y et al (2021) Bioengineered bacteria-derived outer membrane vesicles as a versatile antigen display platform for tumor vaccination via plug-and-display technology. Nat Commun 12(1):2041.
https://doi.org/10.1038/s41467-021-22308-8
29. Hu Y, Li XQ, Zhang Q et al (2021) Exosome-guided bone targeted delivery of antagomir-188 as an anabolic therapy for bone loss. Bioact Mater 6(9):2905–2913.
https://doi.org/10.1016/j.bioactmat.2021.02.014
30. Patel S, Srivastava S, Singh MR et al (2019) Mechanistic insight into diabetic wounds: pathogenesis, molecular targets and treatment strategies to pace wound healing. Biomed Pharmacother 112:108615.
https://doi.org/10.1016/j.biopha.2019.108615
31. Liu J, Chen ZY, Liu H et al (2024) Nickel-based metal-organic frameworks promote diabetic wound healing via scavenging reactive oxygen species and enhancing angiogenesis. Small 20(10):2305076.
https://doi.org/10.1002/smll.202305076
32. Liu H, Qin SM, Zhang HY et al (2025) Silk sericin-based ROS-responsive oxygen generating microneedle platform promotes angiogenesis and decreases inflammation for scarless diabetic wound healing. Adv Funct Mater 35(7):2404461.
https://doi.org/10.1002/adfm.202404461
33. Yang L, Gao YW, Liu QY et al (2024) A bacterial responsive microneedle dressing with hydrogel backing layer for chronic wound treatment. Small 20(12):2307104.
https://doi.org/10.1002/smll.202307104
34. Xu JY, Lin SH, Chen HY et al (2024) Highly active frozen nanovesicles microneedles for senile wound healing via antibacteria, immunotherapy, and skin regeneration. Adv Healthc Mater 13(12):2304315.
https://doi.org/10.1002/adhm.202304315
35. Chen HL, Lan GQ, Ran LX et al (2018) A novel wound dressing based on a Konjac glucomannan/silver nanoparticle composite sponge effectively kills bacteria and accelerates wound healing. Carbohydr Polym 183:70–80.
https://doi.org/10.1016/j.carbpol.2017.11.029
36. Xiang J, Zhu RX, Lang SY et al (2021) Mussel-inspired immobilization of zwitterionic silver nanoparticles toward antibacterial cotton gauze for promoting wound healing. Chem Eng J 409:128291.
https://doi.org/10.1016/j.cej.2020.128291
37. Liu KH, Cheng MQ, Huang H et al (2024) Abalone shell-derived Mg-doped mesoporous hydroxyapatite microsphere drug delivery system loaded with icariin for inducing apoptosis of osteosarcoma cells. Biomater Transl 5(2):185–196.
https://doi.org/10.12336/biomatertransl.2024.02.008
38. Gai YQ, Zhou HJ, Yang YT et al (2024) Injectable body temperature responsive hydrogel for encephalitis treatment via sustained release of nano-anti-inflammatory agents. Biomater Transl 5(3):300–313.
https://doi.org/10.12336/biomatertransl.2024.03.006
39. Liang GF, Kan S, Zhu YL et al (2018) Engineered exosome-mediated delivery of functionally active miR-26a and its enhanced suppression effect in HepG2 cells. int J Nanomed 13:585–599.
https://doi.org/10.2147/IJN.S154458
40. Liu H, Wu Y, Wang FX et al (2023) Bone-targeted engineered bacterial extracellular vesicles delivering miRNA to treat osteoporosis. Compos Part B Eng 267:111047.
https://doi.org/10.1016/j.compositesb.2023.111047
41. Zhang Q, Chen WK, Li GF et al (2024) A factor-free hydrogel with ROS scavenging and responsive degradation for enhanced diabetic bone healing. Small 20(24):2306389.
https://doi.org/10.1002/smll.202306389
42. Semwal RB, Semwal DK, Combrinck S et al (2015) Gingerols and shogaols: important nutraceutical principles from ginger. Phytochemistry 117:554–568.
https://doi.org/10.1016/j.phytochem.2015.07.012
43. Agyepong N, Govinden U, Owusu-Ofori A et al (2018) Multidrug-resistant gram-negative bacterial infections in a teaching hospital in Ghana. Antimicrob Resist Infect Control 7:37.
https://doi.org/10.1186/s13756-018-0324-2
44. Peng H, Li HC, Zhang X et al (2023) 3D-exosomes laden multifunctional hydrogel enhances diabetic wound healing via accelerated angiogenesis. Chem Eng J 475:146238.
https://doi.org/10.1016/j.cej.2023.146238
45. Bao X, Zhu QY, Chen YY et al (2022) Antibacterial and antioxidant films based on HA/Gr/TA fabricated using electrospinning for wound healing. Int J Pharm 626:122139.
https://doi.org/10.1016/j.ijpharm.2022.122139